Nanoscale

# Enhanced motility in a binary mixture of active nano/microswimmers



| | |
|---|---|
| Journal: | *Nanoscale* |
| Manuscript ID | NR-ART-03-2020-001765 |
| Article Type: | Paper |
| Date Submitted by the Author: | 02-Mar-2020 |
| Complete List of Authors: | Debnath, Debajyoti; Presidency University Kolkata, Chemistry<br>Ghosh, Pulak; Presidency University Kolkata, Department of Chemistry ; RIKEN, Theoretical Quantum Physics Laboratory<br>Misko, Vyacheslav R.; Vrije Universiteit Brussel, Department of Chemical Engineering; RIKEN, Theoretical Quantum Physics Laboratory<br>Li, Yunyun; Tongji University, Physics<br>Marchesoni, Fabio; Universita' di Camerino, Dipartimento di Fisica<br>Nori, Franco; Advanced Science Institute, RIKEN, |
| | |

Journal Name

ARTICLE TYPE

Cite this: DOI: 00.0000/xxxxxxxxxx

# Enhanced motility in a binary mixture of active nano/microswimmers

Debajyoti Debnath[1], Pulak Kumar Ghosh[1], Vyacheslav R. Misko[2,3], Yunyun Li[4], Fabio Marchesoni[4], Franco Nori[2,6]

Received Date
Accepted Date

DOI: 00.0000/xxxxxxxxxx

It is often desirable to enhance the motility of active nano- or microscale swimmers such as, e.g., self-propelled JPs as agents of chemical reactions or weak sperm cells for better chances of successful fertilization. Here we tackle this problem based on the idea that motility can be transferred from a more active guest species to a less active host species. We performed numerical simulations of motility transfer in two typical cases, namely for interacting particles with weak inertia effect, by analyzing their velocity distributions, and for interacting overdamped particles, by studying their effusion rate. In both cases we detected motility transfer with a motility enhancement of the host species of up to a factor of four. This technique of motility enhancement can find applications in chemistry, biology and medicine.

## 1 Introduction

Self-propelling Janus particles (JPs), the most common class of artificial microswimmer, have been the focus of widespread attention over the last two decades due to their emerging applications in nano-technology and medical sciences[1–7]. Such particles are made by coating one hemisphere with catalytic or photosensitive or magnetic materials[1,2,4]. Under appropriate conditions, one hemisphere undergoes physical or chemical changes with respect to the other, thus producing some local gradient in the suspension fluid (self-phoresis). This strategy allows artificial swimmers topropel themselves by harvesting energy from their environment.

Thanks to their self-propulsion mechanism and in contrast to their passive peer, artificial swimmers can diffuse orders of magnitude faster[8], are capable of performing autonomous motion in periodic structures with broken spatial symmetry[9–12] and exhibit other peculiar transport properties[13–17]. Inspired by these unique transport features, researchers aim to design customized JPs to be used, for instance, as "nano-robots" capable of performing accurate mechanical operations[18–23]. Additional promising technological applications have also been proposed[1,9,24,32,33]. Among the most appealing ideas being pursued, we mention here the recent attempt to power passive particles through the self-propulsion mechanism of intermediary active particles[9,31–35], to be used as controllable stirrers. In this paper, we numerically study the velocity distribution and effusion of active particles in a binary mixture, to understand how to enhance motility of less active particles by adding more active particles. Mixtures of interacting active particles (either of the same or different kinds) behave quite differently in many ways. For dilute solutions, particles interact via long-range hydrodynamic flows generated by active particles and the short-range interactions can be safely ignored[6]. However, transport properties of dense mixtures are mostly dominated by the short-range interactions, which are responsible for

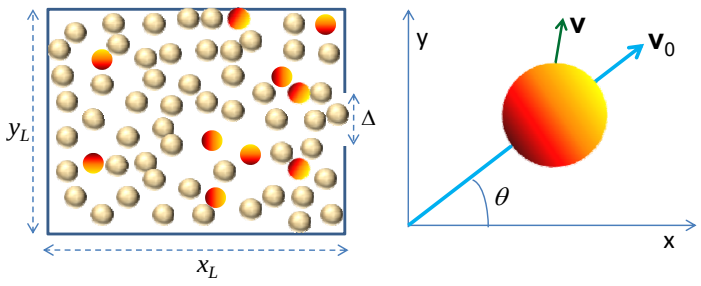


**Fig. 1** (Color online) Left: Schematic of a mixture of self-propelled particles in a rectangular box ($x_L \times y_L$) with an opening of width Δ. Right: Schematic of a two-dimensional self-propelled JP. Its dynamical, $\vec{v}$, and self-propulsion velocities, $\vec{v}_0$, are depicted by distinct vectors.

[1]*Department of Chemistry, Presidency University, 86/1 College Street, Kolkata 700073, India*
[2]*Theoretical Quantum Physics Laboratory, RIKEN Cluster for Pioneering Research, Wako-shi, Saitama 351-0198, Japan*
[3] *μFlow group, Department of Chemical Engineering, Vrije Universiteit Brussel, Pleinlaan 2, 1050 Brussels, Belgium*
[4]*Center for Phononics and Thermal Energy Science, School of Physics Science and Engineering, Tongji University, Shanghai 200092, People's Republic of China*
[5]*Istituto Nazionale di Fisica Nucleare, Sezione di Perugia, I-06123 Perugia, Italy*
[6]*Department of Physics, University of Michigan, Ann Arbor, Michigan 48109-1040, USA*

a variety of cluster and pattern formation processes reported in the recent literature[25–28].

Our simulation of binary active mixtures shows that adding a fraction of active microswimmers, such as self-propelled JPs, to a suspension of passive colloidal particles, results in a motility increase of the latter species. However, adding a small fraction of more active particles to a suspension of less active microswimmers, results in a non-trivial behavior, whereby the added species appears to enhance the motility of the host species. Such a mechanism can be controlled by tuning the parameters ofthe guest species, e.g., the intensity of light in the case of light-induced JP using laser beam[36], near-infrared light[37] or visible light[38,39].

Our findings can be potentially useful for various chemical, biological and medical applications. For example, this technique could be used to increase the rate of *in vitro* fertilization by enhancing the motility of weak sperm cells. The same strategy can be implemented in a chemical reactor to govern the reaction rate, whereby one adds inert active particles to stir otherwise slowly diffusing reactant molecules.

Furthermore, it should be noted that the motility transfer mechanism is associated with some correlated particle dynamics in the mixture. The most sophisticated way to quantify motion correlation of weak and strong active particles is to compute the mixture cooperativity[49]. However, we focus here on the role of cooperativity in controlling the velocity distribution and effusion rates of weak JPs via motility transfer.

The outline of the paper is as follows. In Sec. 2 we present a simple dynamical model for interacting self-propelling JPs in two dimensions, which we implemented in our numerical simulation code. In Sec. 3, we explore the velocity distributions of the two mixture components. We consider first the case of a mixture of two identical species (single species case), of noninteracting, Sec. 3.1, or interacting particles, Sec. 3.2, and, then, the general case of a binary mixture of two different species of interacting active JPs. In Sec. 4, we report our data for the effusion rates of the two JP species out of a narrow opening of the simulation box. Finally, in Sec. 5 we draw a few concluding remarks.

## 2 Model

Let us consider a two-dimensional system consisting of two types of JPs with different self-propulsion speeds in a thermal bath: $N_w$ with speed $v_w$ and $N_s$ with speed $v_s$. In the following, we will refer the subscripts 's' and 'w' to "strong" and "weak" mobility JPs, respectively. All $N = N_w + N_s$ particles are represented by interacting disks of radius $r_0$. For very short distances they interact with each other via a truncated Lennard-Jones potential,

$$\begin{aligned} V_{ij} &= 4\varepsilon\left[\left(\frac{\sigma}{r_{ij}}\right)^{12} - \left(\frac{\sigma}{r_{ij}}\right)^{6}\right], \text{ if } r_{ij} \le r_m \\ &= 0 \text{ otherwise}, \end{aligned} \tag{1}$$

where $\varepsilon$ is the interaction constant, $r_m$ locates the potential minimum, and $\sigma = 2r_0$. Thus, particles interact only through steric repulsion, i.e., no hydrodynamic interactions will be considered here. To illustrate how the motility of the two species are interrelated, we computed two quantifiers, the particles velocity distributions and their effusion rates. However, the former cannot be computed for massless particles (that is in the absence of inertia). Therefore, we assumed damped particle dynamics, although in most practical situations inertia plays no significant role, due to the comparatively very fast viscous relaxation of the suspension medium[40]. One can recover the standard massless, or overdamped, limit by taking very large values of the damping constant $\gamma$. This holds on all physical circumstances when the viscous relaxation time, $1/\gamma$, is much shorter than any other relevant time scale of the system dynamics[42–44].

The dynamics of the particles in the $xy$-plane can be described by the following set of Langevin equations,

$$m\ddot{x}_i = -\gamma[\dot{x}_i + \sum_j F_{ij}^x + v_0\cos\theta_i + \sqrt{D_0}\,\xi_i^x(t)], \tag{2}$$

$$m\ddot{y}_i = -\gamma[\dot{y}_i + \sum_j F_{ij}^y + v_0\sin\theta_i + \sqrt{D_0}\,\xi_i^y(t)], \tag{3}$$

$$\dot{\theta}_i = \xi_i^\theta. \tag{4}$$

The $i$-th particle with instantaneous position $(x_i, y_i)$ diffuses under the combined action of self-propulsion and equilibrium thermal fluctuations. Here, $(\xi_i^x, \xi_i^y)$ are the components of the thermal fluctuations responsible for the particle translational diffusion; they are modeled by Gaussian white noises with $\langle\xi_i^\alpha(t)\rangle = 0$ and $\langle\xi_i^\alpha(t)\xi_i^\beta(0)\rangle = 2\delta_{ij}\delta_{\alpha\beta}\delta(t)$, where $\alpha,\beta = x,y$. The constant $D_0 = kT/\gamma$ can be computed by measuring the translational diffusion of a free JP in the absence of self-propulsion. Here $\gamma$ plays the role of an effective damping constant incorporating all environmental interactions not explicitly accounted for in Eqs. (2)-(3), like fluid viscosity, hydrodynamic drag, surface effects, etc. The second term in the right hand side of the same equations represents the repulsive forces derived from the Lennard-Jones pair potential of Eq. (1).

The propulsion velocities with modulus $v_w$ and $v_s$ are oriented at an angle $\theta_i$ with respect to the laboratory $x$-axis. Due to the particles rotational diffusion, the angles $\theta_i$ change randomly according to the Wiener process of Eq.(4), where $\langle\xi_i^\theta(t)\rangle = 0$ and $\langle\xi_i^\theta(t)\xi_i^\theta(0)\rangle = 2D_\theta\delta(t)$. For a passive particle, the rotational diffusion constant, $D_\theta$, is typically related to the viscosity, $\eta_v$, and temperature, $T$, of the suspension medium and to the geometry of the particle itself[29]. For spherical colloidal particles with radius $r_0$, the rotational diffusion constant can be expressed as $D_\theta = kT/8\pi\eta_v r_0^3$. However, for an active JP rotational diffusion can also depend on the mechanisms fueling its self-propulsion. For this reason, $D_0$, $v_0$, and $D_\theta$ are treated here as independent model parameters[4,5,30]. Moreover, we assumed for simplicity that the noise parameters $D_0$ and $D_\theta$ are the same for both JP species.

From the correlation function, $\langle\cos\theta_i(t)\cos\theta_i(0)\rangle = \langle\sin\theta_i(t)\sin\theta_i(0)\rangle = (1/2)\exp[-D_\theta|t|]$, it is apparent that $D_\theta$ coincides with the rotational relaxation rate of the self-propulsion velocity $\vec{v}_0(t)$. Moreover, we remind that, in the limit of large $\gamma$, a non interacting JP of Eqs. (2)-(4) diffuses normally with translational constant, $D$, consisting of two distinct terms[12],

a thermal and a self-propulsion one, namely $D = D_0 + v_0^2/2D_\theta$.

We numerically integrated Eqs. (2)-(4) using a standard Milstein algorithm to obtain the velocity distributions and effusion rates of the both mixture species. The numerical integration was performed using a very short time step, $10^{-6}$-$10^{-7}$, to ensure numerical stability. Computing the velocity distributions requires no confinement scheme. However, to keep the mixtures densities constant, we set up a simulation box of dimension $x_L \times y_L$ with periodic boundary conditions. Instead, to simulate the effusion rates we assumed that the particles centers are confined inside the simulation box. The particles can then exit the box only through a very small opening of width $\Delta + 2r_0$, to model a pore of accessible width $\Delta$ (see Fig. 1). The opening can be centered anywhere along the box wall. Simulating a confined JP requires defining its collisional dynamics at the boundaries. For the translational velocity $\dot{\vec{r}}$, we imposed elastic reflection, whereas the rotational coordinate, $\theta$, was assumed not to change upon collision (sliding boundary conditions[9]). As a consequence, an active JP tends to slide along the walls until rotational fluctuations, $\xi_\theta$, redirects the particle inside the box. We computed the effusion rate, defined as the number of particles exiting the box through the pore per unit of time, for different particles swimming properties and confinement geometries. At $t = 0$, the particles were uniformly distributed in the box with random orientation. To keep the number density of both species constant, a particle of the same species was re-injected with random position and orientation inside the box, whenever one had escaped through the pore. The running time was set to $10^4 \times \tau_\theta$ or $10^4$, whichever was greater, so as to neglect transient effects due to the initial conditions. The data points reported in the figures shown here have been obtained by ensemble averaging over a minimum of 1000 trajectories. For the simulation parameters values adopted here, the time and length scales are seconds and micrometers, respectively. The mass of a slilica bead of radius 0.75 $\mu$m is taken as a unit of mass. Taking the density[45] of $SiO_2 \approx 2$ g/cm$^{-3}$, the unit of mass would be about $4 \times 10^{-12}$ g. In rescaled units, parameters used in our simulations are consistent with the corresponding values reported in the experimental literature.

## 3 Velocity distribution

It is well known that the velocity of overdamped Brownian particles is an ill-defined quantity. Indeed, massless particles undergo a displacement only during the action of external forces[40], here thermal fluctuations, collisions against other particles or the box walls, and the effective self-propulsion forces[41]. Therefore, to extract a velocity distribution, one needs to simulate inertial effects.

By numerically integrating the coupled Eqs. (2)-(4), we systematically analyzed velocity distributions in systems of non-interacting and interacting active JPs, as well as in binary mixtures of two species of JPs with different self-propulsion speeds.

### 3.1 Velocity distribution of non-interacting active particles

Let us begin with the case of a single species of non-interacting particles self-propelling in a thermal bath of temperature $T$ with speed $v_0$. Velocity distribution at different values of the rotational diffusion constant, $D_\theta$, are shown in Fig. 2. It is apparent that inertial effects become important as the viscous relaxation time constant, $\tau_\gamma = 1/\gamma$, grows comparable or greater than the rotational relaxation time $\tau_\theta = 1/D_\theta$. When $\tau_\gamma \gg \tau_\theta$ (or $\gamma \ll D_\theta$), the velocity distributions are mostly determined by thermal fluctuations. In the opposite regime, $\tau_\gamma \ll \tau_\theta$ (or $\gamma \gg D_\theta$), self-propulsion effects seem to prevail. Hence, the transition from self-propulsion to inertia-dominated regime, clearly emerging from the velocity distributions of Fig. 2

Recall that, as anticipated above, for asymptotically large observation times, a free JP behaves like a persistent Brownian particle with effective temperature[47,48]

$$T_{\rm eff} = \frac{\gamma}{k}\left(D_0 + \frac{v_0^2}{2D_\theta}\right), \tag{5}$$

and persistence length $l_\theta = v_0\tau_\theta$. For suitably large values of $D_\theta$, the self-propulsion length is shorter than the free thermal length, $\sqrt{mkT}/\gamma$, that is $T_{\rm eff} \simeq T$. As a consequence, one expects that the particles velocities must be distributed according to the two-dimensional Maxwellian function,

$$p(v) = \left(\frac{mv}{kT}\right)\exp\left(-\frac{mv^2}{2kT}\right). \tag{6}$$

This assertion is corroborated by the numerical results of Fig. 2(a,b).

A different type of velocity distribution emerges when the self-propulsion length of the active particle is set much larger than its thermal length. The ensuing velocity distribution is governed by the self-propulsion dynamics, its maximum being centered at around $v_0$. Such a distribution results from the combination of the Maxwellian distribution of Eq. (6), and a Gaussian distribution with mean $v_0$ and variance $kT = \gamma D_0$, both due to thermal fluctuations. When lowering the temperature, $T$, the contribution of the Maxwellian part is quickly suppressed, which results in the 2D Gaussian distribution

$$p(v) = \left(\frac{1}{\sqrt{2\pi\gamma D_0}}\right)\exp\left[-\frac{(v-v_0)^2}{2\gamma D_0}\right]. \tag{7}$$

In the zero temperature limit, that is, when translational noise is negligible with respect to rotational noise, this distribution tends to a $\delta$-function centered at $v_0$, whereas the corresponding velocity distributions in one direction become, $p(v_{x,y}) = 1/\pi\sqrt{1-(v_{x,y}/v_0)^2}$. These properties are confirmed by the simulation results displayed in Fig. 2(a) and supplementary FigSM1.

### 3.2 Velocity distribution in a system of interacting active particles

Velocity distributions for different values of the packing fraction, $\phi = 4r_0^2 N_t/(x_L + 2r_0)(y_L + 2r_0)$, are displayed in Fig. 2(b). These distributions are centered at $v_0$ for weakly interacting particles and their center shifts towards lower values with increasing $\phi$. As apparent here, in dense systems, say with $\phi > 0.5$, interacting

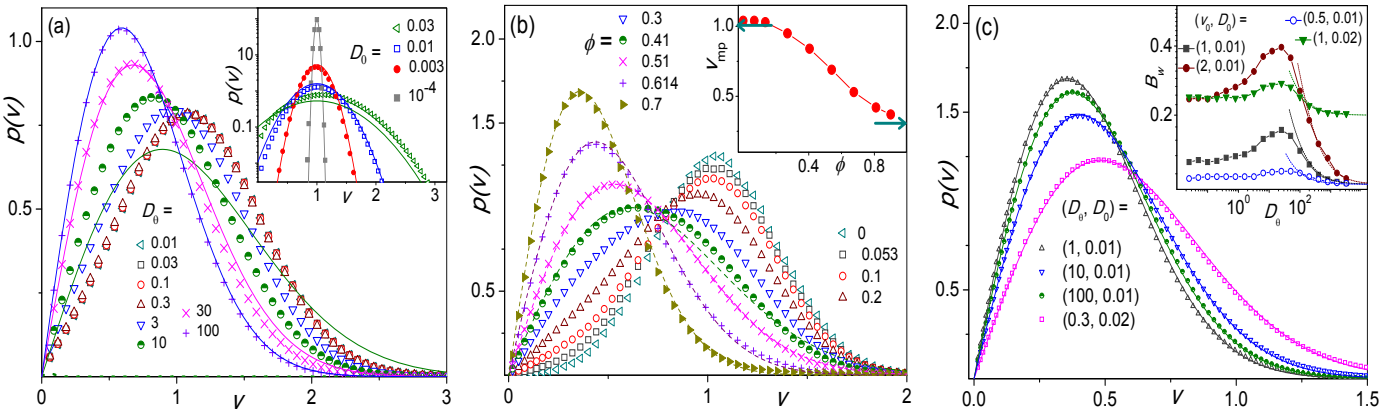


**Fig. 2** (Color online) (a) Velocity distribution of non-interacting active JPs for different $D_\theta$ (see legends). The inset illustrates the effect of thermal noise for $D_\theta = 0.3$. Symbols denote numerical simulation data; solid lines are the analytical estimates of Eq. (6), main panel, and Eq. (7), inset. The parameters used are (unless reported otherwise in the legends): $D_0 = 0.03$, $v_0 = 1$, $\gamma = 10$, $m = 1$. (b)Velocity distribution of interacting self-propelled particles for different the packing fraction, $\phi$. (c)Velocity distribution of interacting self-propelled particles for different $D_\theta$. In the main panels (b) and (c), solid lines represent the least-square fitted 2D Gaussian distributions of Eq.(8). The parameters used are (unless reported otherwise in the legends)): $v_0 = 1$, $\tau_\theta = 3.33, \tau_\gamma = 0.1, r_0 = 0.75$, $D_0 = 0.01$, $\varepsilon = 1$, $\phi = 0.7$. Insets: (b) most probable velocity, $v_{mp}$, versus packing fraction. Asymptotes, at $\phi \to 0$, $v_{\rm mp} \to v_0$ and for $\phi \to 1$, $v_{\rm mp} \to \sqrt{B}$ are depicted by horizontal arrows. (c) Variance of the distribution Eq.(8) as a function of $D_\theta$ for different values of $v_0$ and $D_0$. Dotted lines are analytic curves corresponding to the effective temperature of Eq.(5) (see text).

active JPs obey the Maxwellian velocity distribution,

$$p(v) = \frac{v}{B} \exp\left[-\frac{v^2}{2B}\right], \tag{8}$$

where the fitting parameter, $B$, depends on the bath temperature $T$, the particles rotational diffusion $D_\theta$ and self-propulsion speed $v_0$, and the system packing fraction $\phi$. For $v_0 \to 0$, the distribution is insensitive to the pair interaction, so that $B = \gamma D_0$, like in gas kinetic theory. Therefore, the interaction dependence of the velocity distribution is a non-equilibrium effect of self-propulsion. To examine the impact of self-propulsion on the velocity distribution in a dense system, in Fig. 2(c) we plotted $p(v)$ (main panel) and distribution width $B$ (inset) as a function of $D_\theta$ for different values of the speed $v_0$. One notices immediately that:

(i) For very slow rotational relaxation, the width of the distribution is almost independent of $D_\theta$. In this regime, the self-propulsion length $l_\theta$ is much larger than the average effective inter-particle distance $l_s$, so that the particles free path cannot exceed $l_s$. The fitting parameter seems to obey the empirical law, $B = \gamma\left(D_0 + \alpha v^2\right)$, with $\alpha$ a function of the packing fraction. This result can be explained by comparing $B$ with $kT_{\rm eff}$ in Eq. (5), which we rewrite here as $kT_{\rm eff} = \gamma(D_0 + v_0^2\tau_\theta/2)$. Upon increasing $\phi$, both the mean-free ballistic time $\tau_s = l_s/v_0$ and the mean-free diffusion time $\tau_D = l_s^2/2D_0$ grow larger than the persistence time $\tau_\theta$. As a consequence, $\tau_\theta$ in the above expression for $kT_{\rm eff}$ should now be replaced by $\overline{\tau} = \min\{\tau_s, \tau_D\}$. When the active suspension is so dense that $D_0 > v_0 l_s/2$, then $\overline{\tau} = \tau_D$, so that the fitting parameter $B$ depends quadratically on $v_0$ with $\alpha$ a function of $\phi$.

On a closer look, one notices that $\alpha$ also weakly depends on $v_0$. This is because self-propulsion makes the colliding particles to occasionally overlap, thus slightly lowering the effective $\phi$ value. The pair penetration length and, hence, the effective particles size, can be estimated by equating the self-propulsion force to the inter-particle repulsion.

(ii) In the opposite limit, $l_\theta < l_s$, the active particles manage to change their direction before colliding with other particles, so that their inter-collisional dynamics is dominated by the self-propulsion dynamics. They behave as if they were floating in a thermal bath with the effective temperature of Eq. (5). The ensuing estimates of the distribution fitting parameter, $B = \gamma(D_0 + v^2\tau_\theta/2)$, drawn in the inset of Fig. 2(c) fairly agree with the numerical data.

Figure 2(b,c) [and the supplementary figure FigSM2] also suggests that, under the condition that $v_0^2 \gg B$, the most probable value of $v$, $v_{\rm mp}$, approaches $v_0$. Based on our argument of (i) for dense active suspensions, this requires $v_0^2 \gg \gamma D_0/(1-\alpha)$, with $\alpha = l_s^2\gamma/4D_0$. Of course, this estimate holds only for not too large $\gamma$ values, so that $\alpha < 1$, i.e., for $l_s^2\gamma/4 < D_0$.

(iii) In the intermediate regime, the curves $B$ versus $D_\theta$ exhibit a maximum. Starting with $l_s \ll l_\theta$, as one increases the rotational diffusion constant, self-propulsion enters gradually into play by *enhancing* $B$. On the other hand, self-propulsion effects disappear in the diffusive regime, $l_\theta \ll l_s$, where $B$ decreases with increasing $D_\theta$. Not surprisingly, $B$ appears to reach its maximum in the intermediate regime for $l_\theta$ of the order of the mean inter-particle distance $l_s$.

Finally, it should be noted that the fitting values of $B$ have been extracted by least-square fitting. The fidelity of such fittings has been assessed by computing the mean square weighted deviation[46] $\chi_v^2$. It always returned values close to 1, except for large $v_0$. This deviation is noticeable for $v_0 = 4$, where the rotational diffusion is rather low (shown in supplementary FigSM2).

### 3.3 Velocity distribution in a binary mixture of active particles

Let us consider now a mixture of active particles of two types. Let us denote the $N_w$ particles with fixed self-propulsion speed $v_w$, as *weakly* active, and the remaining $N_s$ particles with tunable

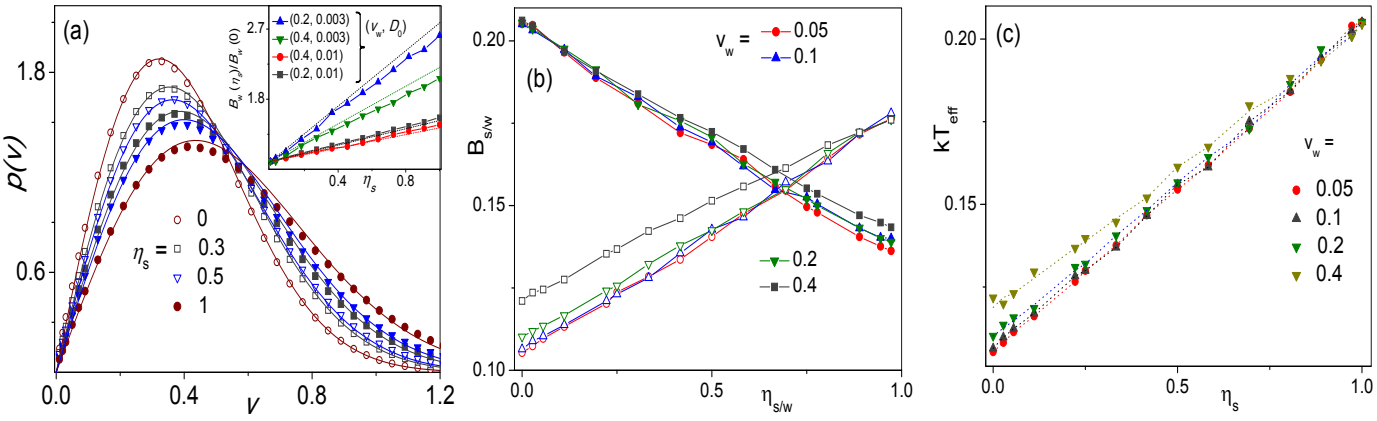


**Fig. 3** (Color online) (a) Comparison of velocity distribution $p(v)$ of weak (empty symbols) and strong (filled symbols) active particles with varying composition $\eta_s$ of the binary mixture. Note that solid (hollow) circles represent velocity distribution of strong (weak) active particles for the interacting single species case. Solid lines correspond to Eq. (8) where $B$ is obtained from least square fittings. Inset plots depict the variation of distribution width of weak JPs $B_w$ as a function of the fraction of strong active particles, $\eta_s = N_s/N_t$. Thus, $\eta_s = 0$ means that all particles are weak and $\eta_s = 1$ that all particles are strong. Dotted lines represent Eq.(9) with the relevant best-fit parameters $\alpha_s$ and $\alpha_w$. (b) Distribution widths of weak, $B_w$ (empty symbols), and strong active JPs, $B_s$ (filled symbols), respectively versus $\eta_s$ and $\eta_w$ for different $v_w$. (c) $kT_{\rm eff}$ versus $\eta_s$ for different $v_w$: numerical data (symbols) are compared with the analytical estimates of Eq. (10) (dotted lines). The remaining model parameters are (unless reported otherwise in the legends): $v_s = 1$, $D_\theta = 0.3, \tau_\gamma = 0.1, r_0 = 0.75$, $D_0 = 0.01$, $\varepsilon = 1$, $\phi = 0.61$.

self-propulsion velocity $v_s$, as *strongly* active. A comparison of velocity distributions of the weak (hollow symbols) and strong (solid symbols) JPs in a binary mixture are shown in Fig. 3(a) for different fractions $\eta_s = N_s/N$ of the strong active particles. Plots here correspond to situations where the system packing fraction $\phi$ is quite large and the velocity distributions $p(v)$ are of the Maxwellian type, Eq. (8). As to be expected, the plots in Fig. 3(a) show that weak active particles distributions grow wider, and their maxima shift to higher velocities, with increasing $\eta_s$. On the other hand, the distributions of the stronger component shrink and their maxima shift toward lower velocity values in comparison with the single component system. This result suggests an effective *motility transfer* from more active to less active particles. To better characterize the underlying mechanism, we estimated the distribution half-widths $B$ for different mixture compositions. The ratio $B_w(\eta_s)/B_w(0)$ in the inset of Fig. 3(a) grows linearly with $\eta_s$, its slope depending on the thermal energy, $kT = \gamma D_0$, and self-propulsion speed of both JP species. This behavior can be explained as follows. Since the system is dense and $l_s \ll l_\theta$, self-propulsion only contributes to the effective thermal motion of the system, see item (i) of Sec. 3.2. Adding up the average kinetic energy contribution from both species and equating the result to the corresponding prediction based on Eq.(8), one can arrive at

$$\frac{B_i(\eta_j)}{B_i(0)} = 1 + \left(\frac{\alpha_j v_j^2 - \alpha_i v_i^2}{\gamma D_0 + \alpha_i v_i^2}\right)\eta_j. \qquad (9)$$

Where, $\{i, j\} = \{s, w\}$ with $i \neq j$. The above estimate rests on the assumption that the self-propulsion contributions to the kinetic energy in this regime are directly proportional to $v_i^2$ with a proportionality constant $\alpha_i$. For $l_s \ll l_\theta$, both $\alpha_i$ are insensitive to the rotational diffusion constant $D_\theta$, and weakly depend on $v_i$. On the contrary, for $l_s \gg l_\theta$, $\alpha_w = \alpha_s = \gamma/2D_\theta$.

To better interpret the mechanism of host-guest mobility transfer, in Fig. 3(b) we compare the widths $B_s$ and $B_w$ of the relevant velocity distributions. We simplify our analysis by focusing on the parameter regimes where both mixture components exhibit a Maxwellian velocity distribution. Figure 3(b) shows that $B_w$ linearly grows as the fraction, $\eta_s$, of strong active particles increases. By contrast, $B_s$ decreases with increasing $\eta_w$. Equation (9) is useful to explain the linear dependence of both $B_s$ and $B_w$ on $\eta_s$. It is apparent from both numerical simulations and Eq. (9) that in a binary mixture the velocity distribution of the weak host depends not as much on its own self-propulsion parameters as on the presence of the strong guest. Under the Maxwellian conditions assumed here, $v_w^2 \ll v_s^2$ and $\gamma D_0 \gg \tau_\theta v_w^2$, one can easily relate the effective temperature of the binary mixture to the distribution widths $B_{s,w}$ as follows,

$$kT_{\rm eff} = (1-\eta_s)B_w(\eta_s) + \eta B_s(\eta_s). \qquad (10)$$

This estimate for $T_{\rm eff}$ is in good agreement with the numerical results shown in Fig. 3(c). In view of the linear $\eta$ dependence of $B$, one would then expect $T_{\rm eff}$ to be a nonlinear function of $\eta$. However, by inspecting Eqs.(9)-(10) one easily concludes that, for the simulation parameters adopted in Fig. 3(c), nonlinear corrections are negligible. As a result, the effective temperature of the binary mixture grows (almost) linearly with the mole fraction of the guest particles. Moreover, Eq. (9) also hints at how the self-propulsion properties of the host and guest particles impact $T_{\rm eff}$.

One often needs to know the fraction of *weakly* active particles whose speed exceeds a specified value, say $v_c$. One can calculate this quantity, $\chi(\eta_s, v_c)$, directly from the velocity distribution function of the less active JPs, that is

$$\chi(\eta_s, v_c) = \int_{v_c}^{\infty} p(v, \eta_s)\, dv. \qquad (11)$$

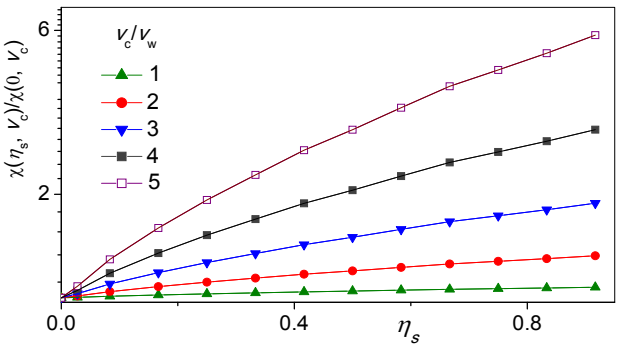


**Fig. 4** (Color online) The ratio, $\chi(\eta_s, v_c)/\chi(\eta_s, v_c)$ versus $\eta_s$ for different $v_c$. The parameters used are (unless mentioned in the legends): $v_s = 1$, $v_w = 0.2$, $D_\theta = 0.3, \tau_\gamma = 0.1, r_0 = 0.75$, $D_0 = 0.01$, $\varepsilon = 1$, $\phi = 0.8$ .

Thus, $\chi(\eta_s, v_c)$ is the fraction of *weakly* active particles having an instantaneous velocity greater than the cut-off velocity $v_c$ in the binary mixture with $N_w$ weak JPs. To clarify the role of $v_c$, we consider the kinetic model of reaction rate theory. As the reactant particles collide with each other, only a certain fraction of such collisions leads to the formation of the desired product. To this purpose it is necessary that the energy of the reactants at the moment of the impact exceeds a threshold value, $E_a$, also known as reaction *activation energy*, which corresponds the the cut-off activation speed, $v_c = \sqrt{2mE_a}$. Therefore, coming back to the problem at hand, it would be desirable to know how the ratio $\chi(\eta_s, v_c)/\chi(0, v_c)$ changes by adding a certain amount of strongly active particles. For the velocity distributions of Eq. (8), such ratio reads

$$\frac{\chi(\eta_s, v_c)}{\chi(0, v_c)} = \exp\left[-\frac{v_c^2}{2}\left(\frac{1}{B(\eta_s)} - \frac{1}{B(0)}\right)\right]. \qquad (12)$$

This quantity, namely the ratio of the number of weakly active JPs with speed larger than $v_c$ to the same number, but in the absence of strongly active JPs, is plotted in Fig. 4 for different values of $v_c$. Our simulations show that $\chi(\eta_s, v_c)/\chi(0, v_c)$ is a monotonically growing function of $\eta_s$; its growth rate increases with increasing $v_c$. These observations support the strategy discussed in Sec. 1 aiming at enhancing the motility of weakly active, or even passive particles, by adding to the system a small fraction of strongly active particles as autonomous stirrers.

## 4 Effusion

In the previous section, we showed how adding a relatively small fraction of highly motile microswimmers to a suspension of less motile microswimmers can considerably enhance the overall motility of the mixture. This effect was demonstrated in the presence of inertia. We consider now the limiting case of overdamped, or massless, active particles. This limit corresponds to low Reynolds numbers, a hydrodynamic regime that applies to most microswimmers investigated in the literature, both biological and artificial. This raises a problem, because, as mentioned above, the velocity distribution of massless particles is mathematically ill-defined. To avoid this difficulty, in our simulations we computed an alternative motility quantifier for the overdamped

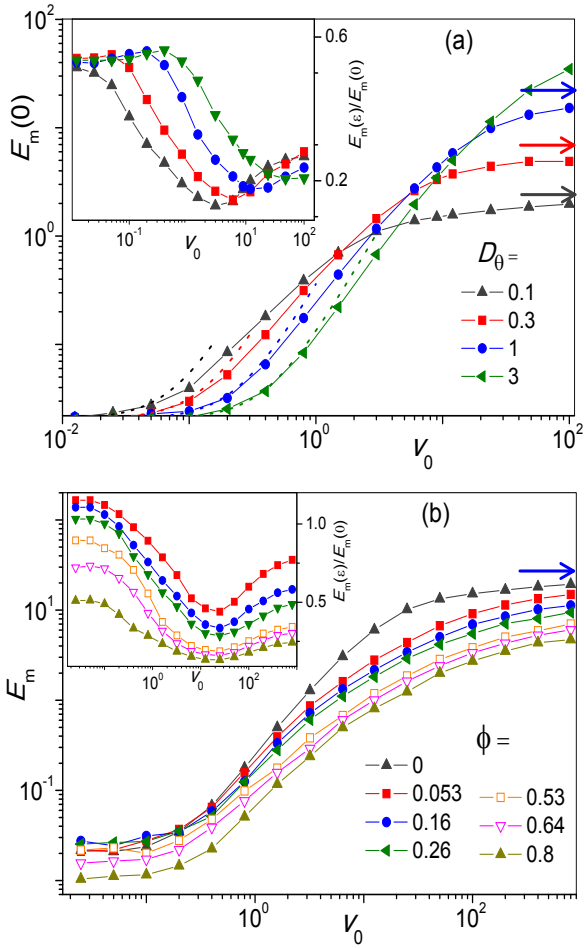


**Fig. 5** (Color online) (a) Effusion rate $E_m(0)$ of non-interacting JPs with $\varepsilon = 0$, as a function of the self-propulsion velocity $v_0$ for different rotational diffusion coefficient $D_\theta$. Dotted lines are the predictions based on Eq. (16). Horizontal arrows indicate the corresponding rate upper bound, Eq. (17), for large $\tau_\theta = 1/D_\theta$. Inset: the effusion rate ratio $E_m(\varepsilon)/E_m(0)$ for $\varepsilon = 0.1$ and different $D_\theta$ (see leends). (b) Effusion rate $E_m(\varepsilon)$ of interacing self-propelled particles versus $v_0$ for $\varepsilon = 1$ and different packing fraction $\phi$. Inset: $E_m(\varepsilon)/E_m(0)$ versus $v_0$ for the same set of parameter as the main panel. Other simulation parameters for main panels and inset: $x_L = y_L = 10$, $\Delta = 0.5, r_0 = 0.5$, $D_0 = 0.03$, $N_m = 80$.

limit, namely the effusion rate of the active JPs through a narrow pore of the simulation box. The corresponding Langevin equations in the highly damped situation are obtained by ignoring inertia in Eqs. (2)-(4),

$$\dot{x}_i = \sum_j F_{ij}^x + v_0 \cos\theta_i + \sqrt{D_0}\,\xi_i^x(t), \qquad (13)$$

$$\dot{y}_i = \sum_j F_{ij}^y + v_0 \sin\theta_i + \sqrt{D_0}\,\xi_i^y(t), \qquad (14)$$

$$\dot{\theta}_i = \sqrt{D_\theta}\,\xi_i^\theta. \qquad (15)$$

The effusion rate has been studied in depth to characterize classical transport in constrained geometries[50]. We define the effusion rate of the *strong* ($s$) [*weak* ($w$)] JPs, $E_s$ ($E_w$), as the number of $s$ ($w$) particles exiting the simulation box per unit time. In the case of a single-component system, we denote the effusion rate by $E_m$.

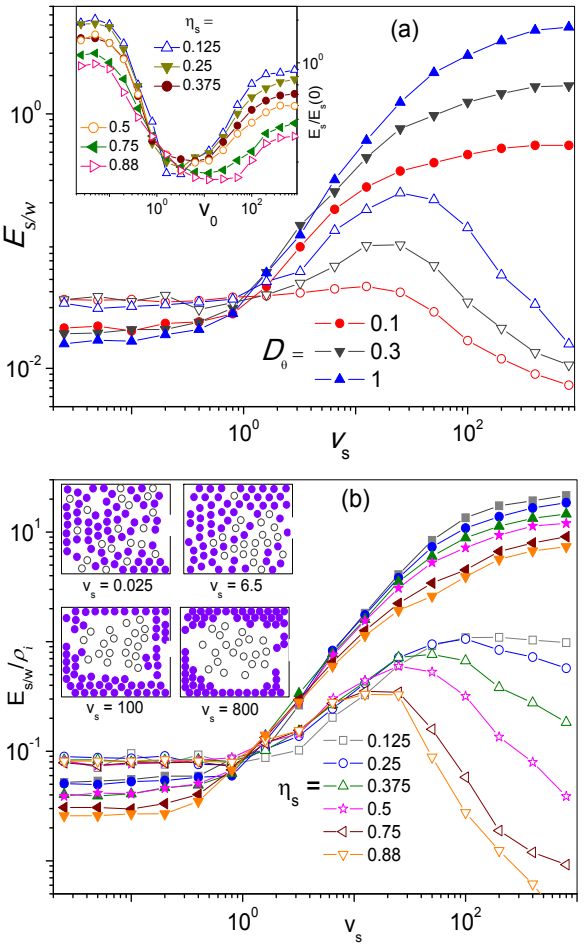


**Fig. 6** (Color online) (a) Effusion rates $E_s$ (filled dots) and $E_w$ (empty dots) versus $v_s$ for binary mixture with $\eta_s = 0.5$ and different values of $D_\theta$ (see legends). Inset: Effusion ratio of stronger component, $E_m(\varepsilon)/E_m(0)$ versus $v_0$ for different $\eta_s$ and $D_\theta = 1$. (b) Effusion rates $E_s$ (filled dots) and $E_w$ (empty dots) versus $v_s$ in a binary mixture for $D_\theta = 1$ and different $\eta_s$ (see legends). Inset: Snapshot of binary mixture with $\eta_s = 0.75$, $D_\theta = 1$ and different $v_s$ [0.025 (top-left), 6.5 (top-right), 100 (bottom-left), and 800 (bottom-right)]. Filled and empty circles represent strong and weak JPs, respectively. Other simulation parameters for main panels and insets: $v_w = 1$, $\varepsilon = 1'$ $x_L = y_L = 10$, $\Delta = 0.5, r_0 = 0.5$, $D_0 = 0.03$, $N_m = 80$

Let us consider the effusion rate $E_m(0)$ of a single species of non-interacting JPs with $\varepsilon = 0$. In Fig. 5(a) we plotted a few curves $E_m(0)$ versus $v_0$ for different values of $D_\theta$. For $v_0 \to 0$, the effusion is controlled by thermal motion and, as expected, is insensitive to $v_0$. Effects due to self-propulsion become appreciable only for values of $v_0$ larger than the particles thermal speed $\sqrt{2D_0 D_\theta}$. Beyond this critical value, the effusion rate grows first quadratically with $v_0$ and then saturates toward an asymptotic value. The rising branches occur for $l_\theta \ll x_L, y_L$. Indeed, for very short rotational relaxation times $\tau_\theta$, when it can safely be assumed that particles diffuse in a thermal bath with effective constant $D_{\rm eff}$, the effusion rate through a narrow pore of effective width $\Delta \ll x_L, y_L$, reads[50–52]

$$E_i = \pi \rho_i D_{\rm eff} \left[ \ln\left( \frac{x_L + y_L}{\Delta} \right) \right]^{-1}. \qquad (16)$$

Here, the suffix $i$ refers to either $s$ or $w$, $\rho_i$ denotes the number density of the mixture component $i$, and $D_{\rm eff}$ is now $D_0 + v_0^2/2D_\theta$ – see Eq.(5). This estimate for $E_i(0)$ agrees fairly closely with the simulation results reported in Fig. 5(a). In the opposite rotational regime, when $l_\theta \gg x_L, y_L$, the slow direction changes of the self-propulsion velocity tends to suppress the particles effusion through the pore. Assuming that $\tau_\theta$ is much larger than any other system time scale, the effusion rate can be approximated by[51]

$$E_i(0) \approx x_L y_L \rho_i D_\theta / \pi. \qquad (17)$$

This asymptotic estimate has been marked in Fig. 5(a) by horizontal arrows.

The effusion rate of interacting self-propelling particles with $\varepsilon > 0$ is plotted in the inset of Fig. 5(a). This figure shows the $v_0$-dependence of the effusion rate relative to the corresponding rate in the absence of interaction, $E_m(\varepsilon)/E_m(0)$, for several values of $D_\theta$. The system we simulated here was quite dense ($\phi = 0.66$), so that the self-propulsion mechanism becomes strongly constrained, being $l_s \ll l_\theta$. Like in non-interacting systems, the effusion rate is insensitive to self-propulsion with low $v_0$. More remarkably, with increasing $v_0$ the relative effusion decreases.

We attributed this result to the jamming of the interacting particles caused by self-propulsion in the vicinity of the box walls. Snapshots of the mixture configurations [see inset of Fig 6(b) and supplementary FigSM3] corroborate this assertion. The jamming effect becomes noticeable as soon as the self-propulsion length becomes larger than the confining box. Therefore, the appearance of such an effect and minima of $E_m(\varepsilon)/E_m(0)$ versus $v_0$ are inversely related to the rotational diffusion [see inset of Fig. 5(a)]. By the same token, one expects that both the decaying and raising branches of the curves $E_m(\varepsilon)/E_m(0)$ versus $v_0$ are quite insensitive to the packing fraction, $\phi$, in agreement with the data plotted in the inset of Fig. 5(b). In the very strong self-propulsion regime, both $E_m(\varepsilon)$ and $E_m(0)$ tend to saturate [see Fig. 5(b)]. However, $E_m(\varepsilon)$ saturates at larger $v_0$ values than in the non-interacting case. A plausible explanation is suggested by a comparison of the mixture snapshots. The particles far away from the walls are more mobile and contribute more to the effusion rate; they are not jammed against the walls and "see" a larger opening-width to compartment-size ratio, $\Delta/y_L$. In contrast, particles jammed against the walls tend to clog the box opening. However, the fraction of the more mobile particles drops fast with increasing $v_0$, thus leading to plateaus in the effusion rate in the limit $v_0 \to \infty$.

Figure 5(b) shows that the clogging mechanism works even at low packing fraction, though its impact on effusion is reduced. More remarkably, the excluded volume effect become apparent for $v_0 \to 0$: the interacting particles become more effusive than the non-interacting ones. In a dilute solution, this effect persists until the self-propulsion length grows larger than the average inter-particle spacing. This explains why, in the presence of strong self-propulsion, the computed effusion ratios still grow with $v_0$, though quite slowly.

Figure 6(a) illustrates the dependence of the effusion rates of the two active mixture components on their self-propulsion pa-

rameters, $v_0$ and $D_\theta$. The mixture is of 1:1 molar ratio of strongly ($s$) and weakly ($w$) active particles. We kept the self-propulsion speed $v_w$ fixed and varied $v_s$ from values lower to values higher than $v_w$. First of all, we notice that the effusion rates of both JP species are almost insensitive to the rotational diffusion for $v_s \to 0$, while develop a strong dependence on $D_\theta$ in the opposite limit, $v_s \to \infty$. For $v_s > 10v_w$, at $D_\theta = 1$ the effusion rate is about one order of magnitude larger than at $D_\theta = 0.1$.

In Fig. 6(b), we examine the consequences of gradually increasing the fraction of guest particles for different values of their self-propulsion speed, $v_s$. While all effusion plots exhibit the same general behavior as in Fig 6(a), a few additional features are remarkable:
(i) The effusion rate of the strongly active JPs keeps increasing, but more slowly than $E_m(0)$ in Fig. 5(a), due to their interaction with the less active JPs. In such a limit, the most active particles tend to push the less active ones against the box walls. Moreover, like in one component systems, clogging effects have great impact on the effusion of both the weak and strong active components.
(ii) On the contrary, the effusion rate of the weak JPs remains unchanged for $v_s$ up to $v_w$; upon further increasing $v_s$, it goes through a maximum in agreement with the mechanism of effective motility transfer. Again, for very large self-propulsion, $v_s \gg x_L D_\theta, x_L D_\theta$, strongly active JPs jam against the container walls, thus pushing the weaker JPs inside [see snapshots of Fig. 6(b) and supplementary FigSM4]. Accordingly, the weaker JPs have a small chance to escape through the opening so that effusion becomes drastically suppressed. Moreover, no decaying branch of $E_w$ *vs.* $v_s$ is detectable at low $\eta_s$. This happens because very few strong JPs cannot possibly confine all weak particles in the box interior.

In conclusion, we stress that adding a small amount of strongly active JPs does suffice to enhance the effusion of sluggish active JPs, but an excess of them can produce the opposite effect! Recall that, as illustrated by our simulation snapshots, the two components of an active binary mixture can separate into two distinct phases, when the self-propulsion length of one component is much larger than the size of the container and the other one much shorter, that is, for $v_s/D_\theta \gg x_L, y_L \gg v_w/D_\theta$. However, phase segregation should be avoided for better motility transfer.

As shown in figure 5(b), there is a window of the tunable $v_s$, where the effusion rate of the $w$ particles is enhanced by 2 to 7 times, depending on their rotational relaxation time and the composition of the binary mixture. Also, the span of this window is sensitive to the persistence length of self-propelled motion. This striking result confirms that, even in the absence of inertia, the *motility of the more active microswimmers can be effectively transferred to the less active microswimmers*.

In our numerical analysis we assumed the pore to be centered in one side of a square-shaped simulation box. However, sliding boundary conditions as the JPs move against the cavity walls, can affect their average effusion rate. Our simulation shows that this may become an issue only at zero temperature. As a matter of fact, thermal fluctuations assist the escape mechanism by enhancing particle diffusion along the boundaries, thus suppressing possible effects related to the cavity geometry and the actual pore location. To verify this point, we simulated the effusion rate (not shown) for a modified box geometry, whereby the escape pore was moved toward one corner; for the simulation parameters of Fig. 5 we detected no appreciable variations of the relevant effusion rates.

## 5 Conclusions

We have analyzed the effects of active nano/micromotors with tunable high motility in a suspension of particles whose motility cannot be directly controlled. We showed that by injecting a small fraction of more active Janus particles one can substantially enhance the motility of other less active species. Such a motility enhancement was demonstrated for two typical cases: particles with weak inertia, by studying the velocity distributions for both species, and for overdamped particles, by comparing their effusion rates.

Our numerical study proves that in dense binary mixtures of active particles, the width of the velocity distribution of the less active particles linearly grows with the fraction of more active particles. Thus, the number of particles moving with larger velocity is considerably enhanced. Moreover, for an appropriate choice of the mixture parameters, in the overdamped regime the motility transfer from the more active to the less active subsystem can raise the effusion rate of the latter by 2 to 7 times.

Such a technique of motility control can be implemented in a large variety of biological and medical situations, where one wishes to enhance the motility of insufficiently active nano- or micro-particles. For example, in the case of weakly motile sperm cells, our proposal has advantages over other similar proposals (e.g., using self-propelled metallic rotors trapping sperm cells[53]), whereby it is substantially less damaging to living swimmers and much easier to implement, as it does not require the fast guest swimmers to localize and trap individual host particles one by one. Another suggestive application of this method of motility transfer is to speed up a chemical reaction involving slowly diffusing nano-particles, by adding a small amount of more active neutral particles as stirrers[54].

## Conflicts of interest

There are no conflicts to declare.

## Accknowledgement

We thank RIKEN Hokusai for providing computational resources. P.K.G. is supported by SERB Start-up Research Grant (Young Scientist) No. YSS/2014/000853 and UGC-BSR Start-Up Grant No. F.30-92/2015. D.D. thanks CSIR, New Delhi, India, for support through a Junior Research Fellowship. V.R.M. and F.N. acknowledge support by the Research Foundation-Flanders (FWO-Vl) and Japan Society for the Promotion of Science (JSPS) (JSPS-FWO Grant No. VS.059.18N). F.N. is supported in part by the: MURI Center for Dynamic Magneto-Optics via the Air Force Office of Scientific Research (AFOSR) (FA9550-14-1-0040), Army Research Office (ARO) (Grant No. Grant No. W911NF-18-1-0358), Japan Science and Technology Agency (JST) (via the Q-LEAP program, and the CREST Grant No. JPMJCR1676), Japan Society for the Promotion of Science (JSPS) (JSPS-RFBR Grant No. 17-52-

50023, and JSPS-FWO Grant No. VS.059.18N), the RIKEN-AIST Challenge Research Fund, the Foundational Questions Institute (FQXi), and the NTT PHI Laboratory.

## References


1 S. Jiang and S. Granick (eds.), *Janus Particle Synthesis, Self-Assembly and Applications* (RSC, Cambridge, 2012).

2 W. F. Paxton, S. Sundararajan, T. E. Mallouk, and A. Sen,*Chemical locomotion*, Angew. Chem. Int. Ed., 2006, **45**, 5420-5429.

3 P. Tierno, *Recent advances in anisotropic magnetic colloids: realization, assembly and applications*, Phys. Chem. Chem. Phys., 2014, **16**, 23515-23528.

4 J. G. Gibbs and Y.-P. Zhao, *Autonomously motile catalytic nanomotors by bubble propulsion*, Appl. Phys. Lett., 2009, **94**, 163104.

5 J. R. Howse, R. A. L. Jones, A. J. Ryan, T. Gough, R. Vafabakhsh, and R. Golestanian, *Self-Motile Colloidal Particles: From Directed Propulsion to Random Walk*, Phys. Rev. Lett., 2007, **99**, 048102.

6 C. Bechinger, R. Di Leonardo, H. Löwen, C. Reichhardt, G. Volpe, and G. Volpe, *Active particles in complex and crowded environments*, Rev. Mod. Phys., 2016, **88**, 045006.

7 S. Ramaswamy, *The Mechanics and Statistics of Active Matter*, Annual Review of Condensed Matter Physics, 2010, **1**, 323-345.

8 G. Volpe, I. Buttinoni, D. Vogt, H.-J. Kummerer, and C. Bechinger, *Microswimmers in patterned environments*, Soft Matter, 2011, **7**, 8810-8815.

9 P. K. Ghosh, V. R. Misko, F. Marchesoni, and F. Nori, *Self-Propelled Janus Particles in a Ratchet: Numerical Simulations*, Phys. Rev. Lett., 2013, **110**, 268301.

10 A. M. Pourrahimi and M. Pumera, *Multifunctional and self-propelled spherical Janus nano/micromotors: recent advances*, Nanoscale, 2018, **10**, 16398-16415.

11 B. Ai and J.-C. Wu, *Transport of active ellipsoidal particles in ratchet potentials*, J. Chem. Phys., 2014, **140**, 094103.

12 X. Ao, P. K. Ghosh, Y. Li, G. Schmid, P. Hänggi and F. Marchesoni, *Active Brownian motion in a narrow channel*, Eur. Phys. J. Special Topics, 2014, **223**, 3227-3242.

13 P. K. Ghosh, P. Hänggi, F. Marchesoni, and F. Nori, *Giant negative mobility of Janus particles in a corrugated channel* , Phys. Rev. E, 2014, **89**, 062115.

14 P. K. Ghosh, Y. Li, F. Marchesoni, and F. Nori, *Pseudochemotactic drifts of artificial microswimmers* Phys. Rev. E, 2015, **92**, 012114.

15 A. Geiseler, P. Hänggi, F. Marchesoni, C. Mulhern, and S. Savel'ev, *Chemotaxis of artificial microswimmers in active density waves*, Phys. Rev. E, 2016, **94**, 012613.

16 H. D. Vuijk, A. Sharma, D. Mondal, J. Sommer, and H. Merlitz, *Pseudochemotaxis in inhomogeneous active Brownian systems*, Phys. Rev. E, 2018, **97**, 042612.

17 B. Liebchen, and H. Löwen, *Optimal navigation strategies for active particles* EPL 2019, **127**, 34003.

18 J. Wang, *Nanomachines: Fundamentals and Applications* (Wiley-VCH, Weinheim, 2013).

19 *Smart Drug Delivery System*, edited by A. D. Sezer (IntechOpen, 2016).

20 H. Yu, A. Kopach, V. R. Misko, A. A. Vasylenko, F. Marchesoni, F. Nori, D. Makarov, L. Baraban, and G. Cuniberti, *Confined catalytic Janus swimmers: geometry-driven rectification transients and directional locking*, Small, 2016, **12**, 5882-5890.

21 Q. Zou, Z. Li, Z Lu and Z. Sun, *Supracolloidal helices from soft Janus particles by tuning the particle softness*, Nanoscale, 2016, **8**, 4070-4076.

22 S. Krishnamurthy, S. Ghosh, D. Chatterji, R. Ganapathy, and A. K. Sood, *A micrometre-sized heat engine operating between bacterial reservoirs*, Nature Physics (2016), **12**, 1134 .

23 T. Debnath and P.K Ghosh, *Activated barrier crossing dynamics of a Janus particle carrying cargo*, Phys. Chem. Chem. Phys. 2018, **20** (38), 25069-25077.

24 I. Malytska, C. Mzire, M. Kielar, L. Hirsch, G. Wantz, N. Avarvari, A. Kuhn, L. Bouffier, *Bipolar Electrochemistry with Organic Single Crystals for Wireless Synthesis of Metal-Organic Janus Objects and Asymmetric Photovoltage Generation*, J. Phys. Chem. C 2017, **121**, 12921-12927.

25 Y. Fily and M. C. Marchetti, *Athermal Phase Separation of Self-Propelled Particles with No Alignment*, Phys. Rev. Lett., 2012, **108**, 235702.

26 I. Buttinoni, J. Bialke, F. Kümmel, H. Löwen, C. Bechinger, and T. Speck, *Dynamical Clustering and Phase Separation in Suspensions of Self-Propelled Colloidal Particles*, Phys. Rev. Lett., 2013, **110**, 238301.

27 F. J. Schwarzendahl and M. G. Mazza, *Hydrodynamic interactions dominate the structure of active swimmers pair distribution functions*, J. Chem. Phys. 2019, **150**, 184902.

28 F. J. Schwarzendahl and M. G. Mazza, *Maximum in density heterogeneities of active swimmers*, Soft Matter 2018, **14**, 4666.

29 H. C. Berg, *Random Walks in Biology* (Pinceton University Press, 1984).

30 S. van Teeffelen and H. Löwen, *Dynamics of a Brownian circle swimmer*, Phys. Rev. E 2008, **78**, 020101 (R).

31 W. Yang, V. R. Misko, F. Marchesoni, and F. Nori, *Colloidal transport through trap arrays controlled by active microswimmers*, J. Phys. Cond. Matter, 2018, **30**, 264004.

32 J. Stürmer, M. Seyrich, and H. Stark, *Chemotaxis in a binary mixture of active and passive particles*, J. Chem. Phys. 2019, **150**, 214901.

33 S. Lu, Y. Ou, and B. Ai, *Ratchet transport of an active-passive mixture chain in confined structures*, Physica A, 2017, **482**, 501-506.

34 F. Hauke, H. Löwen, B. Liebchen, *Clustering-induced velocity-reversals of active colloids mixed with passive particles*, arXiv:1909.09578 (2019).

35 L. Wang and J. Simmchen, *Interactions of Active Colloids with Passive Tracers*, Condens. Matter 2019, **4**(3), 78; https://doi.org/10.3390/condmat4030078

36 H. R. Jiang, N. Yoshinaga and M. Sano, *Active Motion of a Janus Particle by Self-Thermophoresis in a Defocused Laser Beam*, Phys. Rev. Lett., 2010, **105**, 268302.

37 X. Lin, T. Si, Z. Wu and Q. He, *Self-thermophoretic motion of controlled assembled micro-/nanomotors*, Phys. Chem. Chem. Phys., 2017, **19**, 23606-23613.

38 X. Wang, L. Baraban, V. R. Misko, F. Nori, T. Huang, G. Cuniberti, J. Fassbender, and D. Makarov, *Visible Light Actuated Efficient Exclusion Between Plasmonic Ag/AgCl Micromotors and Passive Beads*, Small 2018, **14**, 1802537 (2018). https://doi.org/10.1002/smll.201802537.

39 X. Wang, L. Baraban, A. Nguyen, J. Ge, V. R. Misko, J. Tempere, F. Nori, P. Formanek, T. Huang, G. Cuniberti, J. Fassbender, and D. Makarov, *High Motility Visible Light Driven Ag/AgCl Janus Micromotors*, Small 2018, **14**, 1803613. https://doi.org/10.1002/smll.201803613.

40 C. W. Gardiner, *Handbook of Stochastic Methods*, 2nd ed. (Springer, Berlin, 1985).

41 B. ten Hagen, R. Wittkowski, D. Takagi, F. Kümmel, C. Bechinger, and H. Löwen, *Can the self-propulsion of anisotropic microswimmers be described by using forces and torques?* J. Phys.: Condens. Matter 2015, **27**, 194110.

42 P. K. Ghosh, P. Hänggi, F. Marchesoni, F. Nori, G. Schmid, *Brownian transport in corrugated channels with inertia*, Phys. Rev. E, 2012, **86** (2), 021112.

43 C. Scholz, S. Jahanshahi, A. Ldov, H. Löwen, *Inertial delay of self-propelled particles*, Nature Commun., 2018, **9**, 5156.

44 H. Löwen, *Inertial effects of self-propelled particles: From active Brownian to active Langevin motion*, J. Chem. Phys. 2020, **152**, 040901.

45 W. M. Haynes, (ed.), *CRC Handbook of Chemistry and Physics*, (Boca Raton, FL: CRC Press., 2011).

46 P. R. Bevington, *Data Reduction and Error Analysis for the Physical Sciences*, (New York, McGraw-Hill, 1969), p. 89. For $\chi^2$ tests, $\chi^2_v$ should be approximately equal to one.

47 J. Palacci, C. Cottin-Bizonne, C. Ybert, and L. Bocquet *Sedimentation and Effective Temperature of Active Colloidal Suspensions* Phys. Rev. Lett. 2010, **105**, 088304.

48 J. R. Howse, R. A. L. Jones, A. J. Ryan, T. Gough, R. Vafabakhsh, and R. Golestanian, *Self-Motile Colloidal Particles: From Directed Propulsion to Random Walk*, Phys. Rev. Lett. 2007, **99**, 048102.

49 Adam Wysocki, Roland G. Winkler and Gerhard Gompper, *Cooperative motion of active Brownian spheres in three-dimensional dense suspensions*, EPL 2014, **105**, 48004.

50 D. Holcman and Z.Schuss, *Stochastic Narrow Escape in Molecular and Cellular Biology* (New York, Springer, 2015).

51 P. K. Ghosh, *Communication: Escape kinetics of self-propelled Janus particles from a cavity: Numerical simulations*, J. Chem. Phys., 2014, **141**, 061102.

52 L. Bosi, P. K. Ghosh, and F. Marchesoni *Analytical estimates of free Brownian diffusion times in corrugated narrow channels*, J. Chem. Phys., 2012, **137**, 174110. https://doi.org/10.1063/1.4764297

53 M. Medina-Sanchez, L. Schwarz, A. K. Meyer, F. Hebenstreit, and O. G. Schmidt, *Cellular Cargo Delivery: Toward Assisted Fertilization by Sperm Carrying Micromotors*, Nano Lett., 2016, **16**, 555.

54 S. Sengupta, K. K. Dey, H. S. Muddana, T. Tabouillot, M. E. Ibele, P. J. Butler, and A. Sen, *Enzyme Molecules as Nanomotors*, J. Am. Chem. Soc. 2013, **135**, 1406-1414.